Title

Specialized computational methods for denoising, B1 correction, and kinetic modeling in hyperpolarized 13C MR EPSI studies of liver tumors

Journal

Magnetic Resonance in Medicine, 86(5)

ISSN

0740-3194

Authors

Lee, Philip M

Chen, Hsin-Yu

Gordon, Jeremy W

et al.

Publication Date

2021-11-01

DOI

10.1002/mrm.28901

Peer reviewed

HHS Public Access

Author manuscript

Magn Reson Med. Author manuscript; available in PMC 2021 November 03.

Published in final edited form as:

Magn Reson Med. 2021 November ; 86(5): 2402–2411. doi:10.1002/mrm.28901.

Specialized computational methods for denoising, B_1 correction, and kinetic modeling in hyperpolarized ^{13}C MR EPSI studies of liver tumors

Philip M. Lee[1,2], **Hsin-Yu Chen**[2], **Jeremy W. Gordon**[2], **Zihan Zhu**[1,2], **Peder E.Z. Larson**[1,2], **Nicholas Dwork**[2], **Mark Van Criekinge**[2], **Lucas Carvajal**[2], **Michael A. Ohliger**[2], **Zhen J. Wang**[2], **Duan Xu**[1,2], **John Kurhanewicz**[1,2], **Robert A. Bok**[2], **Rahul Aggarwal**[3], **Pamela N. Munster**[3], **Daniel B. Vigneron**[1,2]

[1]UC Berkeley-UCSF Graduate Program in Bioengineering, University of California, San Francisco and University of California, Berkeley, California, USA

[2]Department of Radiology and Biomedical Imaging, University of California, San Francisco, San Francisco, California, USA

[3]Department of Medicine, University of California, San Francisco, San Francisco, California, USA

Abstract

Purpose: To develop a novel post-processing pipeline for hyperpolarized (HP) ^{13}C MRSI that integrates tensor denoising and B_1^+ correction to measure pyruvate-to-lactate conversion rates (k_{PL}) in patients with liver tumors.

Methods: Seven HP ^{13}C MR scans of progressing liver tumors were acquired using a custom ^{13}C surface transmit/receive coil and the echo-planar spectroscopic imaging (EPSI) data analysis included B_0 correction, tensor rank truncation, and zero-and first-order phase corrections to recover metabolite signals that would otherwise be obscured by spectral noise as well as a correction for inhomogeneous transmit (B_1^+) using a B_1^+ map aligned to the coil position for each patient scan. Processed HP data and corrected flip angles were analyzed with an inputless two-site exchange model to calculate k_{PL}.

Results: Denoising averages SNR increases of pyruvate, lactate, and alanine were 37.4-, 34.0-, and 20.1-fold, respectively, with lactate and alanine dynamics most noticeably recovered and better defined. In agreement with Monte Carlo simulations, over-flipped regions underestimated k_{PL} and under-flipped regions overestimated k_{PL}. B_1^+ correction addressed this issue.

Conclusion: The new HP ^{13}C EPSI post-processing pipeline integrated tensor denoising and B_1^+ correction to measure k_{PL} in patients with liver tumors. These technical developments not only recovered metabolite signals in voxels that did not receive the prescribed flip angle, but also

Correspondence: Philip M. Lee, Department of Radiology and Biomedical Imaging, University of California, San Francisco, 1700 Fourth Street, Byers Hall Suite 102, San Francisco, CA 94158, USA. philip.lee2@ucsf.edu, **TWITTER**: *Philip M. Lee*@_philiplee.

SUPPORTING INFORMATION

Additional Supporting Information may be found online in the Supporting Information section.

increased the extent and accuracy of k_{PL} estimations throughout the tumor and adjacent regions including normal-appearing tissue and additional lesions.

Keywords

analysis; B_1 correction; hyperpolarized ^{13}C-pyruvate MR

1 | INTRODUCTION

Hyperpolarized (HP) ^{13}C MRSI using dissolution dynamic nuclear polarization techniques[1] enables quantitative imaging of enzyme-catalyzed metabolism in humans and has been applied to study in vivo metabolism of cardiac diseases,[2,3] breast cancer,[4,5] brain cancer,[6–9] and prostate cancer.[10–12] In this metabolic imaging approach, HP ^{13}C-pyruvate can be safely injected into human subjects while retaining an observable signal that is 10,000+-fold higher than thermal values at clinical field strengths.[13] Analysis and kinetic modeling can quantify enzymatic conversion rates in key metabolic pathways, most notably the pyruvate-to-lactate conversion through lactate dehydrogenase (LDH).[13–15] The measured rate constant, k_{PL}, is a potential biomarker that is greatly increased in cancer[13,16] and has been shown to reflect treatment response in animal models[17–20] and in humans.[10,12]

Although prior studies demonstrated the ability to detect increased pyruvate-to-lactate conversion in high grade cancers and reduced conversion following successful therapy,[5,7,10,12,17–20] current methods are often sub-optimal with several technical challenges yet to be fully overcome.[13] Background noise in HP spectra can obscure downstream metabolite signals limiting the achievable spatial resolution and reducing the accuracy of k_{PL} estimations in these cases. Surface transmit/receive (T/R) coils can improve SNR limitations increasing the sensitivity in these experiments, but they produce an inhomogeneous transmit (B_1^+) profile. This results in spatially varying flip angles that could bias quantification.[14,21]

The goal of this project was to develop a novel post-processing pipeline to improve spectral SNR using tensor rank truncation denoising and to correct k_{PL} data for B_1^+ variations in human studies of metastatic and primary cancers in the liver. This was designed to enable quantitative HP ^{13}C-pyruvate MR to address an important unmet clinical need for measuring cancer metabolism and response to therapy in liver tumors.

2 | METHODS

2.1 | Patients

Seven MRI exams including a HP ^{13}C MR acquisition were performed on a clinical 3T MRI scanner with multi-nuclear capability from three patients enrolled in a HP MRI study of metastatic cancer. These seven exams are tabulated in Table 1. The human studies were approved by an Institutional Review Board (IRB) requiring informed consent and followed Food and Drug Administration Investigational New Drug application (FDA IND) approved protocols.

2.2 | HP ^{13}C patient MRI scans

The studies were conducted on a clinical 3T MRI (GE Healthcare, Milwaukee, WI) with a custom figure-8 surface coil (shown in Figure 1) for ^{13}C transmit and receive and either a commercial 32-channel torso array or a 16-channel flex array for ^{1}H receive. As seen in Figure 1A, the figure-8 coil measured 17 cm × 10 cm. Vitamin E capsules were embedded in the coil at its corners and along one central axis, and therefore, facilitated coil positioning because they were visible on T_1-weighted images. A ^{13}C-enriched urea phantom was also visible on T_1-weighted images and was used for transmit power calibration. As seen in Figure 1B, both vitamin E capsules and the urea phantom, highlighted by yellow dots, were used during the initial B_1^+ map acquisition and subsequent alignment. Details for the B_1^+ map and correction are presented in section 2.5. Figure 1C–D show an example coil-placement for a patient scan, here with the figure-8 coil and a 32-channel ^{1}H torso array.

Good manufacturing practice (GMP) grade [1-^{13}C]pyruvic acid (ISOTEC Stable Isotope Division, MilliporeSigma, Miamisburg, OH) with trityl radical (GE Healthcare) was prepared and loaded in pharmacy kits (GE Healthcare) according to IRB- and FDA IND-approved stable-isotope manufacturing processes. Following polarization in a 5T SPINLab clinical-research polarizer (GE Healthcare) and dissolution, 240 ± 5.2 mM sterile pyruvate with 7.8 ± 0.2 pH, at 33.9°C ± 1.6°C, and a polarization of 37.7% ± 1.7%, was injected following pharmacist approval at 60.1 ± 9.8 s after dissolution at a rate of 5 mL/s followed by a 20 mL saline flush. The injection volume was determined using the weight-based dose of 0.43 mL/kg (total body weight) with a maximum of 40 mL.

2.3 | Data acquisition

HP ^{13}C data were acquired using a 2D dynamic MR echo-planar spectroscopic imaging (EPSI) pulse sequence consisting of a slice-selective spectral-spatial pulse followed by phase-encode and EPSI readout similar to prior prostate cancer studies.[12,22,23] The scan parameters were as follows: 130 ms/3.5–5.2 ms TR/TE, 1.2- to 3-centimeter slice thickness, 1.2 × 1.2 cm in-plane spatial resolution and 3-second temporal resolution, 60-second acquisition window, 545 Hz spectral bandwidth, and constant flip angles of 10° for pyruvate, 20° for lactate, and 15° for alanine. Acquisition was started 5 s after the injection completed. Each patient was asked to breath-hold for as long as comfortable once the acquisition began. T_1-weighted spoiled gradient-echo ^{1}H images (with 4.0 ms/1.8 ms TR/TE) and T_2-weighted single-shot fast spin echo ^{1}H images (with 545.24 ms/81.662 TR/TE) images were acquired for anatomic references.

2.4 | Denoising

The analysis pipeline began with a B_0 inhomogeneity correction that shifted peaks in the spectral dimension.[15,24] For each voxel, the cross correlation between a standard spectrum and the voxel's spectrum was computed and the index of the maximum value was used to obtain the new pyruvate peak index. The pipeline continued with tensor rank truncation for denoising the HP data.[25,26] The spectral, spatial, and temporal dimensions of HP ^{13}C MRSI data were broken down into principal component fibers using high-order singular value decomposition. Because the chemical shift spectrum, geometric space, and metabolic

dynamics were inherently low rank, the dimensions of the HP ^{13}C MRSI data could be represented by a truncated number of fibers. The optimal number of tensor ranks to preserve in each dimension was computed using a bias-variance tradeoff that balances between spurious artifacts and noise removal.[26] Finally, tensor rank truncation was followed by zero-order and first-order phase corrections and a baseline correction. Metabolite signals were calculated by integrating each peak without any overlap because of the sparsity of the HP ^{13}C spectra. Images were sinc interpolated to a matrix size of 1024 × 1024. Pyruvate and lactate SNR thresholds (defined as the mean of the metabolite's signal divided by the standard deviation of the spectral noise) were implemented to mask out noise. Voxels outside of the coil's sensitive region, determined by the acquired B_1^+ map described below, were removed.

2.5 | B_1^+ transmit field inhomogeneity correction

Prior to the patient studies, a transmit inhomogeneity B_1^+ field map was acquired from a phantom (Figure 1B) using the double angle method (DAM).[27–29] This method calculates a flip-angle map as an indirect measurement of the B_1 excitation field. Two images are acquired, I_1 with the prescribed flip angle α_1 and I_1 with the prescribed flip angle $\alpha_2 = 2\alpha_1$. Other acquisition parameters were kept constant. Using a TR of 3 s, T_1 effects were negligible and the equation below was used to compute the B_1^+ map, $\alpha(r)$:

$$\alpha(r) = \arccos\left(\frac{I_2(r)}{2I_1(r)}\right). \quad (1)$$

The surface coil was strapped to a 25-cm diameter cylindrical ethylene glycol phantom.[30] The ^{13}C center frequency was placed on the central ethylene glycol resonance. The B_1^+ data were acquired using a metabolite-selective sequence with a single-shot echo planar readout, with $\alpha_1 = 30°$ and $\alpha_2 = 60°$, a 20 × 20 matrix zero-filled to 32 × 32, with voxel sizes of 0.875 × 0.875 × 4.0 cm. With two flip angles, a NEX of 100, and a TR of 3 s, the total scan time was 600 s. The B_1^+ map was computed using Eq. (1) and thresholded to remove noise voxels.

Because the fiducial markers were present in T_1-weighted images from the initial DAM acquisition and from subsequent patient scans, each marker had corresponding left, posterior, superior (LPS) coordinates in DICOM images. A least squares estimation method[31,32] was used to compute rotation and translation matrices that would transform the fiducial markers' DAM acquisition LPS coordinates to patient scan coordinates. The B_1^+ map and the ^{13}C images were correspondingly converted from pixels to physical dimensions, matching the LPS coordinate system. The B_1^+ map was transformed as above and interpolated to the resolution of the ^{13}C scans, resulting in a registered B_1^+ map where each ^{13}C voxel corresponded to a B_1^+ scaling factor. This scaling factor, the relative transmit power per voxel, was used to scale the nominal flip angle accordingly. The corrected flip

angle was subsequently provided as a parameter for an inputless two-site exchange model[14] to estimate the forward reaction rate of pyruvate to lactate, or k_{PL}. k_{PL} maps were sinc interpolated to a matrix size of 1024 × 1024. Monte Carlo simulations were used to compute expected k_{PL} variations when varying B_1^+ in 10% increments from −20 to +100% relative to its original value.

3 | RESULTS

3.1 | Patient scans

Seven MR exams including HP ^{13}C were acquired from patients with progressing liver tumors from multiple primary cancers as summarized in Table 1. Representative data from scan 5 are shown in Figures 2 and 3 and were acquired with the coil set-up shown in Figure 1. The conversion of pyruvate-to-lactate in the liver metastases was observed to be upregulated, consistent with the metabolic reprogramming known to occur in cancers.[13,33,34]

3.2 | Denoising and B_1^+ transmit field inhomogeneity correction

The denoising pipeline consisting of B_0 correction, tensor rank truncation, and zero- and first-order phase corrections was applied before B_1^+ correction and k_{PL} analysis for all seven scans with results summarized in Table 1. On average for all the voxels, pyruvate SNR increased by 37.4-fold, lactate SNR increased by 34.0-fold, and alanine SNR increased by 20.1-fold. Figure 2 shows the spectral data before and after denoising for two selected voxels from a patient with metastatic pancreatic cancer to the liver (scan 5). From left to right, the top row shows the acquired EPSI spectra before and after denoising for a tumor voxel and a normal-appearing voxel, respectively. The adjacent T_1-weighted anatomic images highlight the tumors and selected voxels.

Before denoising, there was a high noise floor obscuring the alanine peak. After denoising, both the lactate and alanine peaks were more clearly resolved both spectrally and dynamically through time with SNR increases of 26.2- and 28.9-fold, respectively. The lactate dynamic profile was likewise recovered and smoothed. Because the acquired pyruvate SNR was high, no significant changes in kinetics were observed after denoising. However, the mean pyruvate SNR increase was 58.7-fold. The dynamic curve for pyruvate remained similar pre- and post-denoising, however, the depiction of lactate and alanine dynamics were greatly improved with the denoising pipeline, shown in the bottom row of Figure 2.

For the same scan, the metabolite peaks of interest were integrated to create images of their spatiotemporal distributions shown in Figure 3. For each metabolite, the top row corresponds to pre-denoised spectra and the bottom row to post-denoised spectra, both rows independently normalized for display. Shown on the right are zoomed-in images for each metabolite pre-and post-denoising for the selected time point 18 s from the start of acquisition, corresponding to the peak of the lactate signal. The background noise was most apparent in the lactate and alanine pre-denoised images. In the denoised lactate images, bright voxels at t = 18 s correspond to the increased conversion to lactate in the metastatic

tumors. However, the shape and location of these hot spots were blurred before denoising. These differences are clearly shown in the images on the right of the figure. The alanine signal is also noticeably recovered from a noisy background at t = 21 s. The improvement for pyruvate detection is not as significant because of its high SNR before denoising.

In addition to denoising, this analysis pipeline provided flip angle corrections using a B_1^+ map acquired from a phantom scan to improve k_{PL} estimation (Figure 1B). The B_1^+ map was acquired and calculated using DAM and is shown as a contour map in Figure 1B showing variations in the B_1^+ field. The corresponding color bar indicates the relative power delivered to the region; 100% indicates the region received the prescribed flip angle.

Representative B_1^+ correction data are shown in Figure 4 from a patient with cholangiocarcinoma (scan 3). Figure 4A shows an axial T_1-weighted spoiled gradient-echo anatomic scan with arrows highlighting large tumors. Two tumor voxels were selected, labeled voxel 1 and 2. Figure 4B shows the previously acquired B_1^+ map aligned using the coil's fiducial markers, highlighted in yellow. Figure 4C–D depict the k_{PL} values for voxel 1 before and after B_1^+ correction, respectively. Before B_1^+ correction, the estimated k_{PL} for this voxel was 0.051 s^{-1}. After B_1^+ correction, the estimated k_{PL} was 0.063 s^{-1}. This voxel was over-flipped by 13% resulting in a −19.01% underestimation of k_{PL} without B_1^+ correction. Figure 4E–F depict the k_{PL} values for voxel 2 before and after B_1^+ correction, respectively. Before B_1^+ correction, the estimated k_{PL} for this voxel was 0.080 s^{-1}. After B_1^+ correction, the estimated k_{PL} was 0.066 s^{-1}. This voxel was under-flipped by 13% resulting in a 20.22% overestimation of k_{PL} without B_1^+ correction. These voxels corresponded with the Monte Carlo simulations in that over-flipping resulted in an underestimation of k_{PL} and under-flipping resulted in an overestimation of k_{PL} (Supporting Information Figure S1).

4 | DISCUSSION

HP ^{13}C MRI has been used to quantitatively and dynamically image in vivo metabolic activity in a variety of human studies including cardiac diseases,[2,3] breast cancer,[4,5] brain cancer,[6–9] and prostate cancer.[10–12] Due to metabolic reprogramming, cancer cells demonstrate upregulated expression and activity of LDH,[35,36] the enzyme catalyzing the conversion of pyruvate to lactate, even in the presence of adequate oxygen (the "Warburg effect").[33] Therefore, metabolic conversion from pyruvate to lactate (or k_{PL}) within the cancer cell can serve as a biomarker of tumor characterization,[37] tumor aggressiveness and grading,[11,38–40] metabolic pathway inhibition, and response to drug therapies.[10] In mouse models, HP lactate signals correlated significantly with histologic prostate cancer grade as expected with increased LDH activity.[38,40] Furthermore, the metabolic flux of pyruvate to lactate intratumorally has been shown to be a biomarker of response to therapy.[17–19] Notably, changes in cancer HP [1-^{13}C]pyruvate metabolism has been shown to be a more sensitive biomarker of early response to therapy compared to [^{18}F]FDG-PET in preclinical

models.[20] In human studies, HP [1-^{13}C]pyruvate MR has been used to interrogate metabolism in healthy volunteers[2,41–43] and cancer patients, investigating metabolic reprogramming in primary tumors and metastases.[5–7,10,12,22,44–47] These studies demonstrated that k_{PL} can serve as a biomarker and provide insight into the reprogrammed metabolism of tumors, elucidate response to therapy, and afford the ability to look at cancer progression and aggressiveness.

Differing from prior studies, this new project was designed to develop specialized methods to investigate liver tumor metabolism in patients using HP [1-^{13}C]pyruvate. The goal of the project was to characterize these liver metastases, requiring a dedicated surface coil for acquisition. However, surface coils have an inherently inhomogeneous B_1^+ profile resulting in flip angles that vary through space. B_1^+ correction is especially important for studying inter- and intra-tumor heterogeneity and/or comparing cancerous tissue to normal-appearing tissue. Hence, for the first time, we implemented a B_1^+ correction method within a denoising pipeline for improved spectral SNR using a figure-8 T/R ^{13}C surface coil.

Monte Carlo simulations were computed to elucidate the relationships between B_1^+ error and k_{PL} estimations in the inputless model. All excitations of each time point were consolidated into a single effective flip angle.[14] As seen from the Monte Carlo simulations presented in Supporting Information Figure S1, inaccuracies in k_{PL} estimations arise when it is assumed that all voxels receive the same prescribed nominal flip angle when in reality, there is non-negligible variation of power as a function of space. Hence, to more accurately estimate rates of conversion, namely the first-order conversion rate of pyruvate to lactate (k_{PL}), one must use a B_1^+ map to scale each voxel's flip angle correspondingly. In this work, we developed a novel EPSI processing pipeline that appends B_1^+ correction after a series of spectral processing steps: B_0 inhomogeneity corrections, tensor rank truncation to improve metabolite SNR, and zero- and first-order phase corrections.

In processing the HP ^{13}C EPSI data, the spectral data were denoised before B_1^+ correction. The spectra pre- and post-denoising of a representative voxel are shown in Figure 2. On average, pyruvate, lactate, and alanine SNRs were improved by 37.4-, 34.0-, and 20.1-fold in the spectral dimension, respectively, therefore, substantially recovering metabolite dynamics. This is most noticeable with the lactate and alanine peaks, which are either slightly above or entirely shrouded by the noise floor. By removing extraneous ranks primarily in the frequency dimension of the HP ^{13}C MRSI tensor, low signal metabolites can be extracted for improved subsequent kinetic modeling. The denoised lactate dynamics shown in Figure 2 also more accurately reflected physiological expectations. Compared to the pre-denoised dynamics, the post-denoised dynamics have an elongated lactate plateau beginning from around 18 s until 40 s. With the liver's dual input blood supply from the hepatic artery and the portal vein, we should expect a sustained lactate peak as the portal vein, which delivers two-thirds of the liver's blood supply, brings HP ^{13}C lactate produced by the gastrointestinal tract to the liver. This physiological phenomenon is not as clearly perceptible before denoising and is reflected in the denoised dynamics. The denoised spectra were also

corrected for B_1^+ field inhomogeneities before modeling metabolite dynamics in each voxel. A previously measured B_1^+ map using DAM was used to scale the nominal flip angle for each voxel. The corrected flip angles with the denoised spectra were provided as parameters for an inputless two-site model to estimate k_{PL}. The corrected k_{PL} values were compared against the expected changes derived from Monte Carlo simulations in which B_1^+ was varied. As shown in Supporting Information Figure S1, the corrected k_{PL} values fit closely to the ±1 SD bounds and match the inverse relationship between relative B_1^+ error and fractional k_{PL} error: positive errors in B_1^+ resulted in underestimations of k_{PL} and negative errors resulted in overestimations.

The developed methods here not only restored quantitative accuracy in regions receiving excess or insufficient RF power because of transmit field inhomogeneity, but more importantly increased the number of available voxels outside of the B_1-calibrated region of interest for k_{PL} estimations both in other lesions and in normal-appearing tissue. Limitations of the methods developed in this project include the need for prior mapping of the B_1^+ inhomogeneity profile specific to the coil. Recent real-time power calibration and B_1^+ mapping[48] could improve this approach for the future.

5 | CONCLUSIONS

In this project, a specialized HP ^{13}C EPSI post-processing pipeline was developed that integrated tensor denoising and B_1^+ correction to measure k_{PL} conversion rates in patients with liver tumors, in order to improve the quantitative accuracy of surface coil HP ^{13}C metabolic MR in cancer patients. This approach could benefit future clinical trials using HP ^{13}C MRSI to measure cancer metabolism and response to targeted drug therapies.

Supplementary Material

Refer to Web version on PubMed Central for supplementary material.

ACKNOWLEDGMENTS

This work was supported by NIH grants R01CA183071, U01EB026412, R01DK115987, and P41EB013598. The authors acknowledge the assistance of Jasmine Hu, Jim Slater, Mary Frost, Hope Williams, Kimberly Okamoto, and Jennifer Chow.

Funding information

National Institutes of Health, Grant/Award Numbers: R01CA183071, U01EB026412, R01DK115987, and P41EB013598

REFERENCES

1. Ardenkjær-Larsen JH, Golman K, Gram A, et al. Increase of signal-to-noise of more than 10,000 times in liquid state NMR. Discov Med. 2003;100:10158–10163.
2. Cunningham CH, Lau JYC, Chen AP, et al. Hyperpolarized 13C metabolic MRI of the human heart: initial experience. Circ Res. 2016;119:1177–1182. [PubMed: 27635086]

3. Rider OJ, Apps A, Miller JJJJ, et al. Noninvasive in vivo assessment of cardiac metabolism in the healthy and diabetic human heart using hyperpolarized 13C MRI. Circ Res. 2020;126:725–736. [PubMed: 32078413]
4. Abeyakoon O, Latifoltojar A, Gong F, et al. Hyperpolarised 13C MRI: a new horizon for non-invasive diagnosis of aggressive breast cancer. BJR Case Rep. 2019;5:20190026.
5. Gallagher FA, Woitek R, McLean MA, et al. Imaging breast cancer using hyperpolarized carbon-13 MRI. Proc Natl Acad Sci USA. 2020;117:2092–2098. [PubMed: 31964840]
6. Park I, Larson PEZ, Gordon JW, et al. Development of methods and feasibility of using hyperpolarized carbon-13 imaging data for evaluating brain metabolism in patient studies. Magn Reson Med. 2018;80:864–873. [PubMed: 29322616]
7. Miloushev VZ, Granlund KL, Boltyanskiy R, et al. Metabolic imaging of the human brain with hyperpolarized 13C Pyruvate demonstrates 13C lactate production in brain tumor patients. Cancer Res. 2018;78:3755–3760. [PubMed: 29769199]
8. Autry AW, Gordon JW, Carvajal L, et al. Comparison between 8- and 32-channel phased-array receive coils for in vivo hyperpolarized 13 C imaging of the human brain. Magn Reson Med. 2019;82:833–841. [PubMed: 30927300]
9. Mammoli D, Gordon J, Autry A, et al. Kinetic modeling of hyperpolarized carbon-13 pyruvate metabolism in the human brain. IEEE Trans Med Imaging. 2020;39:320–327. [PubMed: 31283497]
10. Aggarwal R, Vigneron DB, Kurhanewicz J. Hyperpolarized 1-[13C]-pyruvate magnetic resonance imaging detects an early metabolic response to androgen ablation therapy in prostate cancer. Eur Urol. 2017;72:1028–1029. [PubMed: 28765011]
11. Granlund KL, Tee S-S, Vargas HA, et al. Hyperpolarized MRI of human prostate cancer reveals increased lactate with tumor grade driven by monocarboxylate transporter 1. Cell Metab. 2020;31:105–114. [PubMed: 31564440]
12. Chen H-Y, Aggarwal R, Bok RA, et al. Hyperpolarized 13C-pyruvate MRI detects real-time metabolic flux in prostate cancer metastases to bone and liver: a clinical feasibility study. Prostate Cancer Prostatic Dis. 2020;23:269–276. [PubMed: 31685983]
13. Kurhanewicz J, Vigneron DB, Ardenkjaer-Larsen JH, et al. Hyperpolarized 13C MRI: path to clinical translation in oncology. Neoplasia (United States). 2019;21:1–16.
14. Larson PEZ, Chen H-Y, Gordon JW, et al. Investigation of analysis methods for hyperpolarized 13C-pyruvate metabolic MRI in prostate cancer patients. NMR Biomed. 2018;31:e3997. [PubMed: 30230646]
15. Crane JC, Gordon JW, Chen HY, et al. Hyperpolarized 13C MRI data acquisition and analysis in prostate and brain at University of California, San Francisco. NMR Biomed. 2021;34:e4280. [PubMed: 32189442]
16. Wang ZJ, Ohliger MA, Larson PEZ, et al. Hyperpolarized 13C MRI: state of the art and future directions. Radiology. 2019;291:273–284. [PubMed: 30835184]
17. Day SE, Kettunen MI, Gallagher FA, et al. Detecting tumor response to treatment using hyperpolarized 13C magnetic resonance imaging and spectroscopy. Nat Med. 2007;13:1382–1387. [PubMed: 17965722]
18. Chaumeil MM, Ozawa T, Park IW, et al. Hyperpolarized 13C MR spectroscopic imaging can be used to monitor Everolimus treatment in vivo in an orthotopic rodent model of glioblastoma. Neuroimage. 2012;59:193–201. [PubMed: 21807103]
19. Radoul M, Chaumeil MM, Eriksson P, Wang AS, Phillips JJ, Ronen SM. MR studies of glioblastoma models treated with dual PI3K/mTOR inhibitor and temozolomide: metabolic changes are associated with enhanced survival. Mol Cancer Ther. 2016;15:1113–1122. [PubMed: 26883274]
20. Hesketh RL, Wang J, Wright AJ, et al. Magnetic resonance imaging is more sensitive than PET for detecting treatment-induced cell death–dependent changes in glycolysis. Cancer Res. 2019;79:3557–3569. [PubMed: 31088837]
21. Walker CM, Fuentes D, Larson PEZ, Kundra V, Vigneron DB, Bankson JA. Effects of excitation angle strategy on quantitative analysis of hyperpolarized pyruvate. Magn Reson Med. 2019;81:3754–3762. [PubMed: 30793791]

22. Nelson SJ, Kurhanewicz J, Vigneron DB, et al. Metabolic imaging of patients with prostate cancer using hyperpolarized [1–13C] Pyruvate. Sci Transl Med. 2013;5:198ra108.
23. Chen HY, Larson PEZ, Gordon JW, et al. Technique development of 3D dynamic CS-EPSI for hyperpolarized 13 C pyruvate MR molecular imaging of human prostate cancer. Magn Reson Med. 2018;80:2062–2072. [PubMed: 29575178]
24. Larson PE, Bok R, Kerr AB, et al. Investigation of tumor hyperpolarized [1–13C]-pyruvate dynamics using time-resolved multiband RF excitation echo-planar MRSI. Magn Reson Med. 2010;63:582–591. [PubMed: 20187172]
25. Brender JR, Kishimoto S, Merkle H, et al. Dynamic imaging of glucose and lactate metabolism by 13 C-MRS without hyperpolarization. Sci Rep. 2019;9:3410. [PubMed: 30833588]
26. Chen HY, Autry AW, Brender JR, et al. Tensor image enhancement and optimal multichannel receiver combination analyses for human hyperpolarized 13C MRSI. Magn Reson Med. 2020;84:3351–3365. [PubMed: 32501614]
27. Stollberger R, Wach P, McKinnon G, et al. RF-filed mapping in vivo. In: Proceedings of the 7th Annual Meeting of SMRM, San Francisco, CA, USA. 1988, p. 106.
28. Insko E, Bolinger L. B1 mapping. In: Proceedings of the 11th Annual Meeting of SMRM, Berlin, Germany. 1992, p. 4302.
29. Cunningham CH, Pauly JM, Nayak KS. Saturated double-angle method for rapid B1+ mapping. Magn Reson Med. 2006;55:1326–1333. [PubMed: 16683260]
30. Hansen RB, Sánchez-Heredia JD, Bøgh N, et al. Coil profile estimation strategies for parallel imaging with hyperpolarized 13C MRI. Magn Reson Med. 2019;82:2104–2117. [PubMed: 31297868]
31. Jacobsen M Absolute Orientation -Horn's method. MATLAB Central File Exchange. Published 2020. https://www.mathworks.com/matlabcentral/fileexchange/26186-absolute-orientation-horn-s-method
32. Ohliger MA, Gordon JW, Carvajal L, et al. 55Mn-based fiducial markers for rapid and automated RF coil localization for hyperpolarized 13C MRI. Magn Reson Med. 2021;85:518–530. [PubMed: 32738073]
33. Warburg O On the origin of cancer cells. Science (80-). 1956;123:309–314.
34. Vander Heiden MG, DeBerardinis RJ. Understanding the intersections between metabolism and cancer biology. Cell. 2017;168:657–669. [PubMed: 28187287]
35. Hu S, Balakrishnan A, Bok R, et al. 13C-pyruvate imaging reveals alterations in glycolysis that precede c-Myc-induced tumor formation and regression. Cell Metab. 2011;14:131–142. [PubMed: 21723511]
36. Keshari KR, Sriram R, Van Criekinge M, et al. Metabolic reprogramming and validation of hyperpolarized 13C lactate as a prostate cancer biomarker using a human prostate tissue slice culture bioreactor. Prostate. 2013;73:1171–1181. [PubMed: 23532911]
37. Sriram R, Van Criekinge M, Santos JD, et al. Non-invasive differentiation of benign renal tumors from clear cell renal cell carcinomas using clinically translatable hyperpolarized 13C pyruvate magnetic resonance. Tomography. 2016;2:35–42. [PubMed: 27227168]
38. Albers MJ, Bok R, Chen AP, et al. Hyperpolarized 13C lactate, pyruvate, and alanine: noninvasive biomarkers for prostate cancer detection and grading. Cancer Res. 2008;68:8607–8615. [PubMed: 18922937]
39. Sriram R, Van Criekinge M, Hansen A, et al. Real-time measurement of hyperpolarized lactate production and efflux as a biomarker of tumor aggressiveness in an MR compatible 3D cell culture bioreactor. NMR Biomed. 2015;28:1141–1149. [PubMed: 26202449]
40. Serrao EM, Kettunen MI, Rodrigues TB, et al. MRI with hyperpolarised [1–13C]pyruvate detects advanced pancreatic preneoplasia prior to invasive disease in a mouse model. Gut. 2016;65:465–475. [PubMed: 26347531]
41. Grist JT, McLean MA, Riemer F, et al. Quantifying normal human brain metabolism using hyperpolarized [1–13 C]pyruvate and magnetic resonance imaging. Neuroimage. 2019;189:171–179. [PubMed: 30639333]
42. Lee CY, Soliman H, Geraghty BJ, et al. Lactate topography of the human brain using hyperpolarized 13C-MRI. Neuroimage. 2020;204:116202. [PubMed: 31557546]

43. Gordon JW, Autry AW, Tang S, et al. A variable resolution approach for improved acquisition of hyperpolarized 13C metabolic MRI. Magn Reson Med. 2020;84:2943–2952. [PubMed: 32697867]
44. Gordon JW, Chen H-Y, Autry A, et al. Translation of Carbon-13 EPI for hyperpolarized MR molecular imaging of prostate and brain cancer patients. Magn Reson Med. 2019;81:2702–2709. [PubMed: 30375043]
45. Tran M, Latifoltojar A, Neves JB, et al. First-in-human in vivo non-invasive assessment of intra-tumoral metabolic heterogeneity in renal cell carcinoma. BJR|case reports. 2019;5:20190003.
46. Stødkilde-Jørgensen H, Laustsen C, Hansen ESS, et al. Pilot study experiences with hyperpolarized [1–13C]pyruvate MRI in pancreatic cancer patients. J Magn Reson Imaging. 2020;51:961–963. [PubMed: 31368215]
47. Autry AW, Gordon JW, Chen H-Y, et al. Characterization of serial hyperpolarized 13C metabolic imaging in patients with glioma. NeuroImage Clin. 2020;27:102323. [PubMed: 32623139]
48. Tang S, Milshteyn E, Reed G, et al. A regional bolus tracking and real-time B1 calibration method for hyperpolarized 13C MRI. Magn Reson Med. 2019;81:839–851. [PubMed: 30277268]

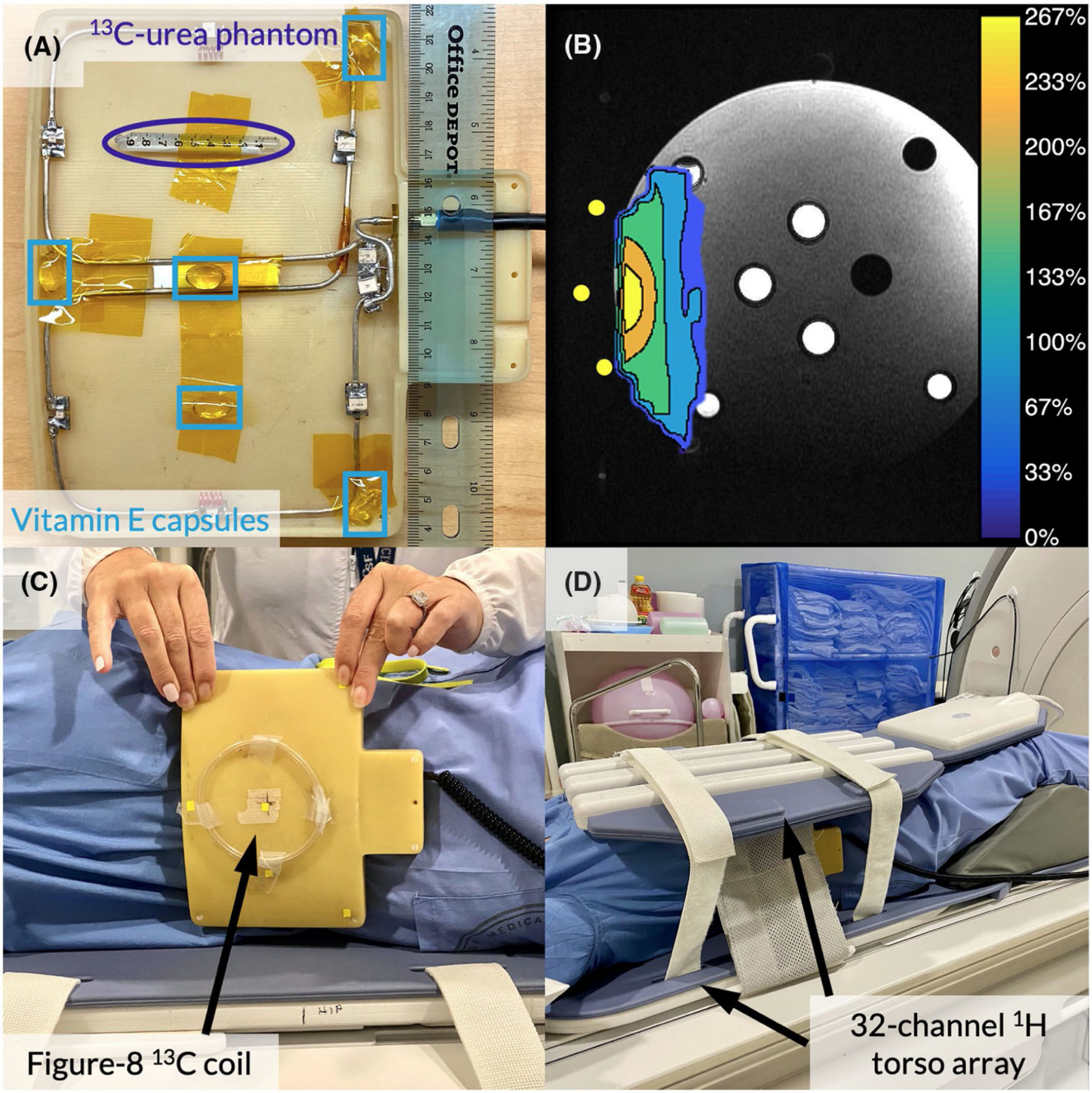

FIGURE 1.

(A) The figure-8 T/R coil opened with a ^{13}C-enriched urea phantom used for power calibration highlighted by a purple circle and vitamin E capsule fiducial markers highlighted by light blue rectangles. (B) The coil's B_1^+ profile acquired using the double angle method. The contour map indicates the actual flip angle delivered relative to the prescribed flip angle. (C and D) Photos of an example coil-placement for a patient scan. Exterior markers were used for verifying coil placement following localizer scans, but were not used for B_1^+ correction.

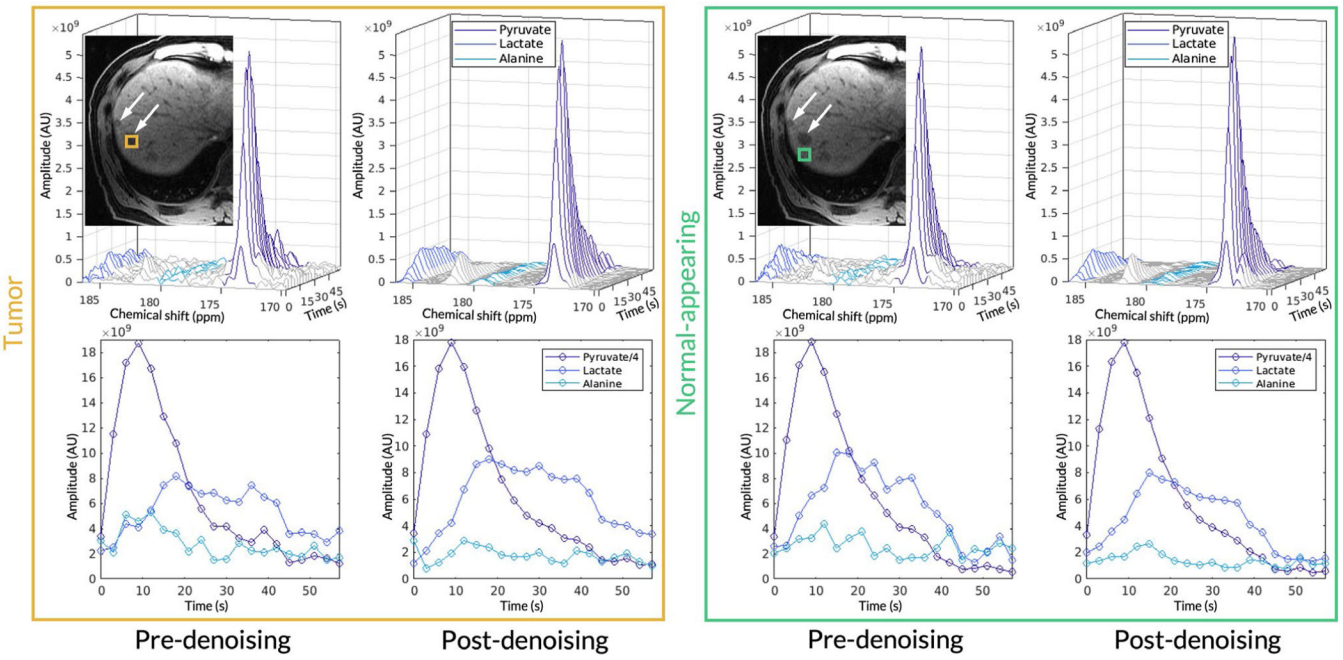

FIGURE 2.

The left panel (orange box) shows the acquired HP ^{13}C EPSI spectrum and metabolite dynamics before and after denoising for the tumor voxel. Likewise, the right panel (green box) shows the acquired EPSI spectrum and metabolite dynamics before and after denoising for a normal-appearing voxel. The adjacent T_1-weighted anatomic images highlight locations of the metastases and the selected voxel. Both are representative voxels taken from scan 5.

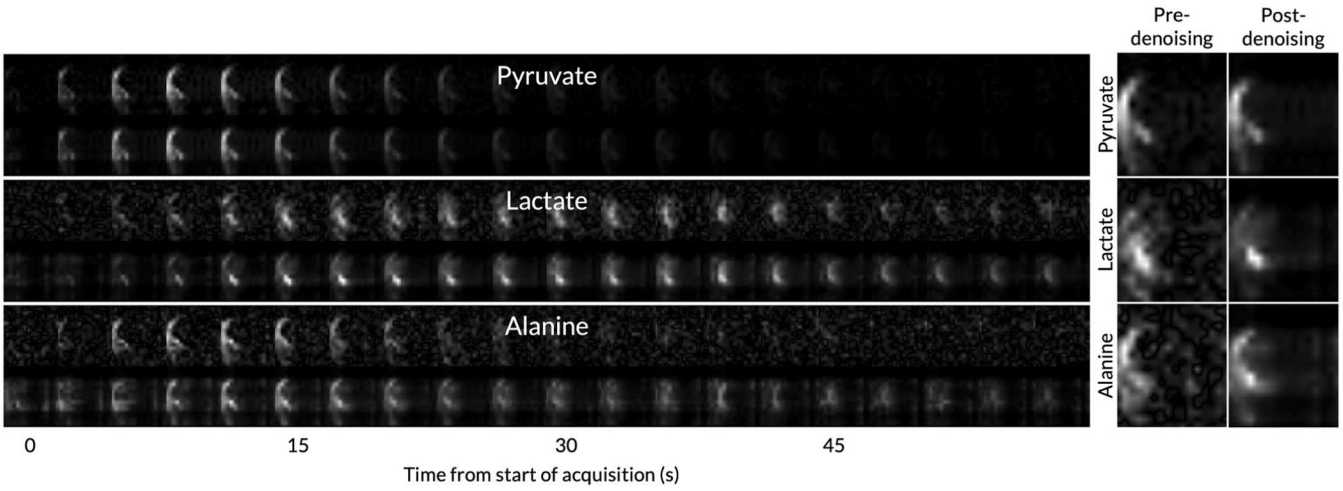

FIGURE 3.

From scan 5, the metabolite peaks from pyruvate, lactate, and alanine were integrated and the resulting time courses are shown on the left side of the figure. For each metabolite, the top row of images is from the original spectra and the bottom row of images shows the post-denoised metabolite maps. Every entire row of images is independently window-leveled relative to the other rows. On the right are displayed zoomed-in images before and after denoising for a selected time point (18 s from the start of acquisition) are highlighted on the right side of the figure.

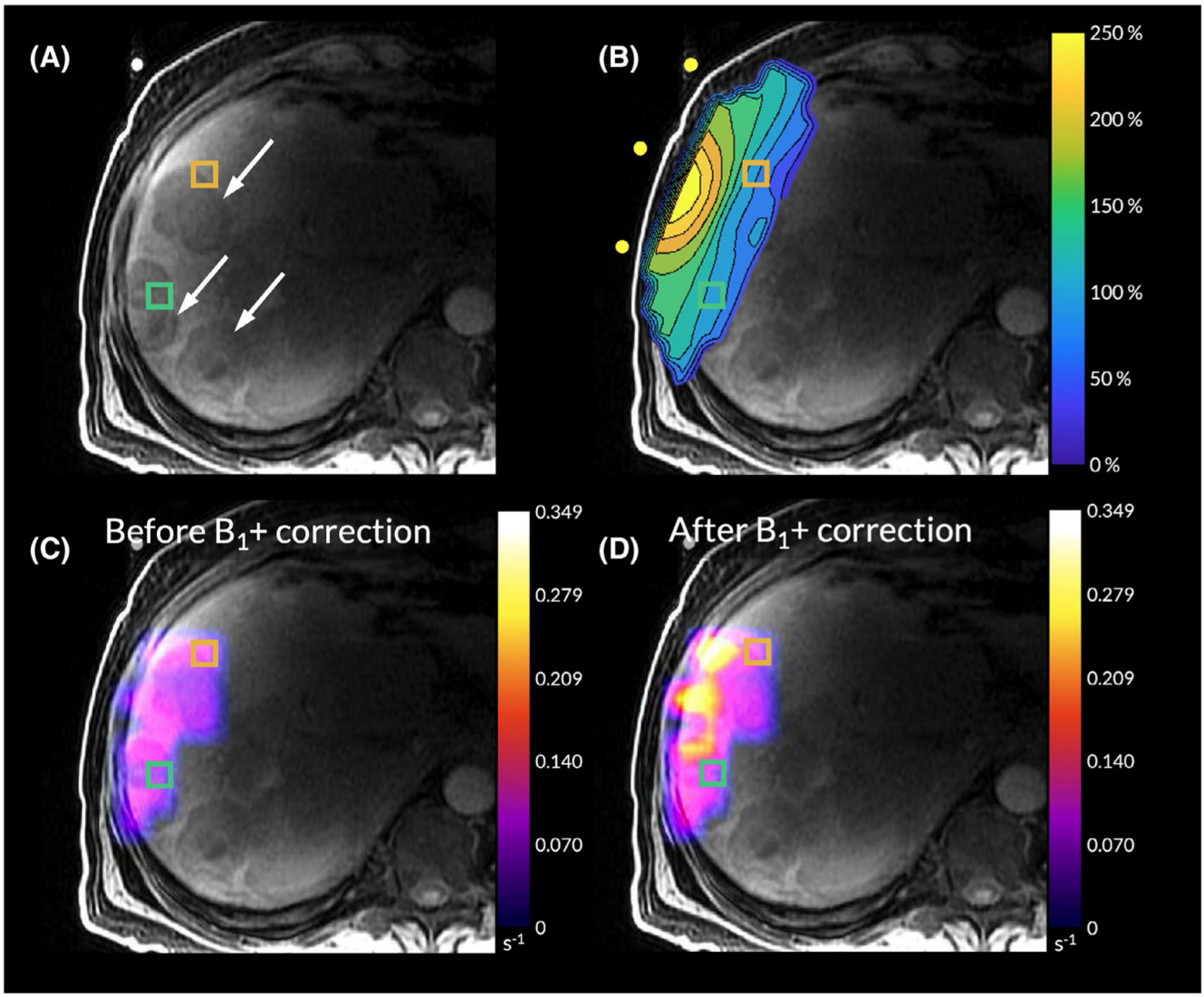

FIGURE 4.

From scan 3, (A) an axial T_1-weighted spoiled gradient-echo anatomic scan with an over-flipped tumor voxel highlighted in green (voxel 1) and an under-flipped tumor voxel highlighted in orange (voxel 2). (B) The B_1^+ profile aligned to its position during the scan using the coil's fiducial markers. (C) The k_{PL} map before B_1^+ correction. (D) The k_{PL} map after B_1^+ correction. For voxel 1, over-flipped by +13%, there was a −19.01% underestimation of k_{PL} without B_1^+ correction (0.051 s^{-1} before denoising and 0.063 s^{-1} after denoising). For voxel 2, under-flipped by −13%, there was a +20.22% overestimation of k_{PL} without B_1^+ correction (0.080 s^{-1} before denoising and 0.066 s^{-1} after denoising).

TABLE 1

Selected voxels from seven patient scans showing the optimized tensor ranks (with dimensions: frequency, x, y, and time), improvements in SNR after denoising, the flip correction scaling factor (over-flipped: >1, under-flipped: <1), the k_{PL} values before and after B_1^+ correction, and the % difference

Scan no.	Cancer origin and notes	Optimized tensor ranks [freq, x, y, t]	Denoising SNR multiplicative increases	Flip angle scaling	k_{PL} before correction (s^{-1})	k_{PL} after correction (s^{-1})	% Difference
1	Rectal adenocarcinoma	[18, 9, 10, 5]	Pyr: 17.5	1.20	0.031	0.042	−27.96
			Lac: 9.4	1.03	0.038	0.040	−4.60
			Ala: 4.0	1.10	0.044	0.052	−15.24
2	Rectal adenocarcinoma	[12, 8, 11, 8]	Pyr: 15.9	0.97	0.044	0.042	+5.77
			Lac: 20.2	1.03	0.037	0.039	−5.58
			Ala: 9.1	1.13	0.033	0.042	−19.49
3	Intrahepatic cholangiocarcinoma	[7, 5, 11, 18]	Pyr: 26.5	1.13	0.051	0.063	−19.01
			Lac: 27.6	0.87	0.080	0.066	+20.22
			Ala: 35.1	0.97	0.051	0.048	+5.31
4	Intrahepatic cholangiocarcinoma	[5, 6, 8, 6]	Pyr: 82.4	1.37	0.030	0.053	−43.62
			Lac: 101.8	1.27	0.048	0.073	−34.79
			Ala: 17.7	1.17	0.043	0.057	−23.64
5	Recurrent grade 1 metastatic pancreatic neuroendocrine	[14, 8, 5, 7]	Pyr: 58.7	0.97	0.043	0.040	+5.64
			Lac: 26.2	0.97	0.029	0.027	+5.60
			Ala: 28.9	1.03	0.024	0.026	−5.38
6	Recurrent grade 1 metastatic pancreatic neuroendocrine	[10, 7, 14, 3]	Pyr: 47.9	1.27	0.043	0.069	−37.65
			Lac: 42.3	0.87	0.059	0.047	+26.96
			Ala: 37.5	0.97	0.049	0.046	+6.21
7	Recurrent grade 1 metastatic pancreatic neuroendocrine	[20, 7, 12, 7]	Pyr: 12.6	1.27	0.041	0.066	−37.86
			Lac: 10.4	0.97	0.038	0.036	+5.90
			Ala: 8.7	0.97	0.032	0.031	+5.84

There were variations between the SNR gains of the metabolite peaks, where larger SNR gains were shown in those with lower SNR dynamic spectra before denoising.